

Towards ultra-thin imaging systems: an optic that replaces space

Orad Reshef^{1,*}, Michael P. DelMastro¹, Katherine K. M. Bearn¹, Ali H. Alhulaymi¹, Lambert Giner^{1,2}, Robert W. Boyd^{1,3,4}, and Jeff S. Lundeen¹

¹Department of Physics, University of Ottawa, 25 Templeton Street, Ottawa, ON K1N 6N5, Canada

²National Research Council of Canada, Ottawa, ON K1A 0R6, Canada

³School of Electrical Engineering and Computer Science, University of Ottawa, Ottawa, ON K1N 6N5, Canada

⁴Institute of Optics and Department of Physics and Astronomy, University of Rochester, Rochester, New York 14627, USA

*e-mail: orad@reshef.ca

Centuries of effort to improve imaging has focused on perfecting and combining lenses to obtain better optical performance, such as achromatic lenses, and new functionalities, such as microscopy¹. The arrival of nanotechnology has now enabled thin subwavelength-structured surfaces called metalenses, which promise to make imaging devices more compact². However, unaddressed by this promise is the space *between* the lenses, which is crucial for image formation but takes up by far the most room in imaging systems. Here, we address this issue by presenting the concept and demonstration of an optical ‘spaceplate’ that effectively propagates light for a length that can be considerably longer than the plate thickness. Such propagation compression produces signatures that we experimentally observe in three common situations in optics: first, in the focusing of a beam; second, in the transverse translation of a beam incident at an angle; and lastly, in image formation. Whereas metalenses and essentially all other optical components act on the complex light field at each transverse position (*i.e.*, locally^{3–7}), a spaceplate operates directly on the transverse momentum of the field (*i.e.*, non-locally^{8–10}). Specifically, the spaceplate reproduces the Fourier transfer function that describes the propagation of light through a homogeneous isotropic dielectric slab (*e.g.*, a slab of vacuum)¹¹ by shifting the optical phase as a function of the wave’s direction. This concept promises to dramatically compress the length of all imaging systems and opens the possibility for ultra-thin flat monolithic cameras. It also breaks the current constraint between image sensor size and field-of-view and, thus, between pixel size and image resolution, enabling ultra-large pixels for high-sensitivity. More broadly, a spaceplate can be applied to miniaturize important devices that implicitly manipulate the spatial profile of light, for example, solar concentrators, collimators for light sources, integrated optical components, and spectrometers^{12–14}.

Metasurfaces — engineered surfaces consisting of sub-wavelength scatterers — have attracted a great deal of attention for enabling flat optical components^{3–7,15}. These devices have been implemented in a diverse set of novel linear^{16–20} and nonlinear optical^{21–23} applications, including sub-wavelength-scale broadband achromatic lenses²⁴, the generation of various transverse spatial modes^{3,17}, lasing^{25,26}, polarimetry²⁷, and holograms²⁸, among others. Notably, metalenses are seen as the most promising by far due to their impact in miniaturizing imaging systems^{2,29}. However, in all imaging systems, lenses represent just one of the two main components; the other, often overlooked, is the mm-to-m-scale optical propagation surrounding the lenses and separating them from the object and image. As evidenced by the long length of a typical telescope, the distance between lenses is just as critical to image formation as the lenses themselves, and can easily be greater than the lenses’ combined thickness by an order of magnitude. To date, no metasurface or metamaterial has been proposed to address this dominant contribution to the

overall size of all optical systems.

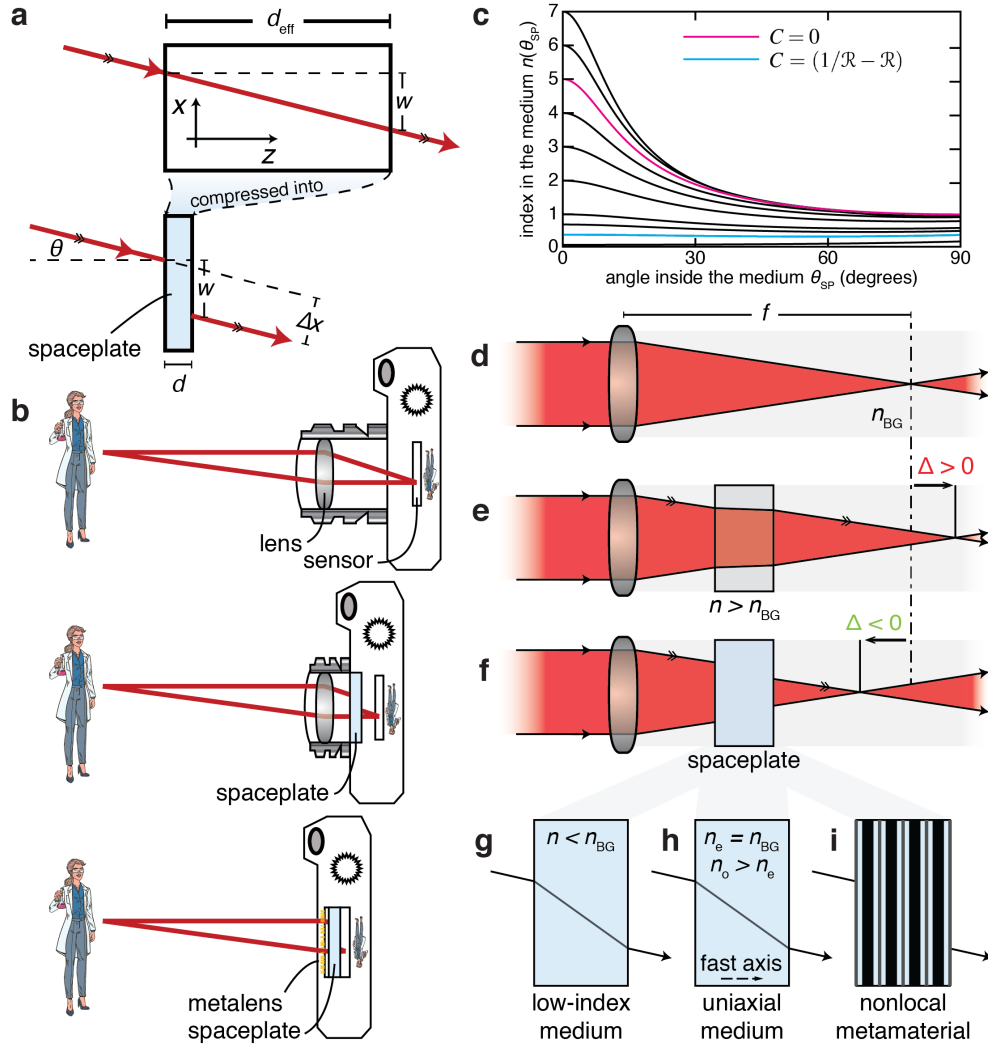


Fig. 1 | Operating principle of a spaceplate. **a**, A spaceplate can compress a propagation length of d_{eff} into a thickness d . For example, a beam incident on the spaceplate at angle θ will emerge at that same angle and be transversely translated by length w (resulting in a lateral beam shift Δx), just as it would for d_{eff} of free space. **b**, Adding a spaceplate to an imaging system such as a standard camera (top) will shorten the camera (center). An ultrathin monolithic imaging system can be formed by integrating a metalens and a spaceplate directly on a sensor (bottom). **c**, A spaceplate can be made of a homogeneous medium with any of these angle-dependent refractive index curves. **d**, A lens focuses a collimated beam at a working distance corresponding to its focal length f . **e**, The physical distance to the point of focus is increased by a length Δ when a plane-parallel plate with a refractive index n that is larger than that of the background medium n_{BG} is inserted into the beam path. The emerging rays are parallel to the original incident rays, which preserves the lens strength. **f**, A spaceplate will act to *advance* the point of focus while also preserving the lens strength. The plate therefore effectively propagates light for a longer length than the physical space it occupies. This effect can be achieved using **(g)** a plane-parallel plate with a refractive index $n < n_{\text{BG}}$, or **(h)** for the extraordinary ray for propagation along the fast axis (e) of a uniaxial birefringent medium with $n_{\text{BG}} = n_e$, or **(i)** using a nonlocal metamaterial.

We present a solution to reduce the size of these remaining regions in the form of an optical element that we call a ‘spaceplate’. The functionality of a spaceplate is highlighted in Fig. 1a— this element would occupy a physical thickness of d while propagating light for an effective length of $d_{\text{eff}} > d$, where the ratio between these two quantities $\mathcal{R} \equiv d_{\text{eff}}/d$ is the compression factor of the plate. In particular, a spaceplate produces the same transverse displacement of a beam (parallel to the surface, labeled as w in Fig. 1a) as that of a longer propagation length d_{eff} . Critical to the operation of a spaceplate is that upon transmission, it preserves propagation angle θ — rays exiting the plate are parallel to their corresponding incoming rays. This criterion ensures that the plate will not introduce any additional lens power (*i.e.*, magnification) to the image. For these reasons, the spaceplate is a fundamentally new type of optical element that is inherently different than, for example, curved mirrors, filters, or lenses.

The application of a spaceplate to miniaturizing a camera is illustrated in Fig. 1b. The space between the lens and the sensor of a camera is dictated to a large degree by the focal length f of the lens. A relatively large focal length is necessary to suitably magnify an image, which leads to long lens barrels in cameras. Integrating a spaceplate into a camera allows for the magnification of a faraway object without the need for a proportional propagation length, thereby breaking the trade-off between lens barrel length and image magnification. Since the resulting image may now be large, so can the image sensor (*e.g.*, the charge-coupled device (CCD) array). One can capitalize on this larger sensor by using larger pixels for low-light sensitivity, or a greater number of pixels for a higher resolution. In this way, the spaceplate also breaks the trade-off between camera miniaturization and resolution or sensitivity. Most promising, both a spaceplate and a metalens can be integrated directly on top of a sensor to enable a true ultra-thin monolithic camera. There are many optical devices that implicitly use imaging (*e.g.*, a grating spectrometer works by imaging a slit¹⁴) or that manipulate light using its propagation, such as solar concentrators¹², multiplane mode demultiplexers³⁰, or multi-mode interferometers in integrated optics¹³. All of these devices can be shortened by a spaceplate.

We use the perspective of Fourier optics to consider what space does to each plane-wave that composes the incident field, that is, to any given spatial Fourier component at momentum vector \vec{k} . The amplitude of each k -vector component is preserved in its free-space propagation whereas the phase is shifted. Consider two points along z separated by d_{eff} in a given plane-wave. The wave’s phase difference between these points will be $\phi = k_z d_{\text{eff}}$, where $k_z = |\vec{k}| \cos \theta$, and θ is the angle of \vec{k} to the z -axis. Combining this amplitude and phase behaviour, the Fourier transfer function of free space is $H(\vec{k}) = \exp(ik_z d_{\text{eff}})$. Therefore, the spaceplate should produce the same transfer function.

We consider spaceplate designs that are translationally invariant along the transverse directions x and y . This invariance guarantees that a transmitted wave will have the same k -vector as the incident wave, which is a necessity for $|H| = 1$. Returning to phase, with $|\vec{k}| = (2\pi n_{\text{BG}}/\lambda)$ we find $\phi = (2\pi n_{\text{BG}} d_{\text{eff}} \cos \theta / \lambda) \equiv \phi_{\text{BG}}$, where λ is the wavelength of light in vacuum and n_{BG} is the index of the medium in the d_{eff} slab of space. The critical action of a spaceplate is to produce an angle-dependent phase profile ϕ_{SP} that is equal to $\phi_{\text{BG}}(\theta, d_{\text{eff}})$, but within a distance shorter than d_{eff} (in particular, in a plate thickness d). Note that there are two parameters in the angular phase profile ϕ_{SP} that do not affect the imaging properties of the plate. The first is the addition to ϕ_{SP} of an arbitrary phase offset ϕ_{G} that is global, *i.e.*, it is independent of θ ²⁹. Second, ϕ_{SP} may be discontinuous as a function of θ , with discontinuities of an integer multiple m of 2π ; this type of solution would correspond to the Fourier-space analogue of a Fresnel lens^{31,32}. These two free parameters hint at the substantial flexibility available to design a spaceplate. Below, we elaborate on three examples of spaceplate designs that use different operating mechanisms to impart this angularly-dependent phase.

We first consider whether the spaceplate could be a homogeneous optical medium, such as glass. In an interferometer situated in a vacuum background ($n_{\text{BG}} = 1$), a glass plate of index $n = 1.5$ and thickness d

can replace the ‘optical path length’ $d_{\text{eff}} = 1.5d$ of interferometer arm length. Contrast this with the action of the same glass plate on the focus location of a beam propagating in vacuum, as depicted in Figs. 1d-e. Counter to the intuition derived from the interferometer, refraction at the plate boundaries makes the focus shift *further* along the propagation direction, as if it had passed through distance $d_{\text{eff}} = (n_{\text{BG}}/n)d = (d/1.5)$ in vacuum³³. This is the opposite effect to what we seek, showing that the established concept of optical path length is not appropriate for a spaceplate. Instead, we aim to tailor the requisite angle-dependent phase response ϕ by introducing an angle-dependent refractive index. We solve for the required profile of the refractive index as a function of the k -vector angle within the medium θ_{SP} to find

$$\frac{n(\theta_{\text{SP}})}{n_{\text{BG}}} = \frac{C + \sqrt{C^2 + (\mathcal{R}^2 - C^2)(1 + \mathcal{R}^2 \tan^2 \theta_{\text{SP}})}}{(1 + \mathcal{R}^2 \tan^2 \theta_{\text{SP}}) \cos \theta_{\text{SP}}}, \quad (1)$$

where $C = (\phi_{\text{G}} + 2\pi m(\theta_{\text{SP}}))/\phi_{\text{BG}}(0, d)$ (see Sec. S2: [Homogeneous spaceplate solutions](#) for details). Such a medium is homogeneous but non-isotropic. If the refractive index of a plate varies in this way then the plate will appear a factor \mathcal{R} greater propagation distance than its thickness. That is, the plate acts as a spaceplate for a background medium with refractive index n_{BG} .

We now discuss the requisite index profile in more detail and identify two solutions that are physically realizable. From here on, we assume $m = 0$ for all angles. Since ϕ_{G} is still arbitrary, so is C . Thus, C parametrizes an infinite family of solutions, some of which are shown in Fig. 1c. We first focus on the $C = (1/\mathcal{R} - \mathcal{R})$ solution (Fig. 1g). It gives an spaceplate index that is lower than that of the background medium for all angles, $n(\theta_{\text{SP}}) < n_{\text{BG}}$. It is also the flattest of any solution near $\theta_{\text{SP}} = 0$ and, thus, corresponds to an approximately isotropic medium $n(\theta_{\text{SP}}) \equiv n_{\text{LI}}$, particularly for small incident angles. This is similar to the glass plate discussed above, but now the index of the plate n_{LI} is *less* than that of the background medium n_{BG} , so $d_{\text{eff}} = (n_{\text{BG}}/n_{\text{LI}})d$ is greater than d . For this low-index spaceplate, $\mathcal{R} = (n_{\text{BG}}/n_{\text{LI}})$. If the background medium is vacuum, then n_{LI} must be less than one, a seemingly unusual property. Nonetheless, there exist both natural and metamaterials (*e.g.*, epsilon-near-zero (ENZ) materials) from which such a spaceplate can be made³⁴. With this low-index spaceplate the beam focus is shifted *towards* the plate, as if the beam had propagated through an additional length of the background medium, effectively reducing the required distance along z (Fig. 1f).

The second realizable homogeneous solution is the one for which $C = 0$ (Fig. 1h). Since this solution has no global phase offset ($\phi_{\text{G}} = 0$), not only will it act as a spaceplate for imaging, it will also replace d_{eff} in an interferometer. This solution is related to but is distinct from a solution from transformation optics that compresses the full electromagnetic field^{35–37}. Remarkably, the refractive index described by this solution is that of a negative uniaxial birefringent medium ($n_{\text{o}} > n_{\text{e}}$ for ordinary (o) and extraordinary (e) polarizations) with its e-axis along z . A light field with e-polarization propagating through this medium experiences a compression factor of $\mathcal{R} = (n_{\text{o}}/n_{\text{e}})$ along z . While it is possible that not every member of the family of index profile solutions is physically possible, the feasibility of these two suggests that there may be more types of homogeneous spaceplates to be found (see Sec. S2.1: [General solution for an angle-dependent refractive index](#) for a discussion of other solutions).

We now experimentally demonstrate the action of these two types of spaceplates, low-index and uniaxial, before moving on to a third non-homogeneous type. We begin with the low-index spaceplate. Current low-index ($n < 1$) materials are prohibitively lossy³⁴, so instead of vacuum, we select a background medium with a higher refractive index, linseed oil (which has $n_{\text{BG}} = 1.48$), and use air as the low-index medium. The low-index plate is a $d = 4.4$ -mm-long cylinder containing air and faced with glass coverslips (see Sec. S3: [Fabricated spaceplates](#)). With air as the low index medium ($n_{\text{LI}} = 1$), the resulting compression factor is $\mathcal{R} = 1.48$. We propagate a focusing beam through the oil and compare it to the same beam when propagating through the low-index plate placed in the oil. An ideal spaceplate will shift this

focus by $\Delta \equiv d - d_{\text{eff}} = -(\mathcal{R} - 1)d$. Looking at Fig. 2a, the addition of the low-index plate clearly shifts the focus towards plate. The measured shift $\Delta = -2.3$ mm, which agrees well with the predicted shift of $\Delta = -2.1$ mm. We repeat this measurement with our other type of spaceplate, the uniaxial crystal. We use a $d = 29.84$ -mm-long calcite crystal (CaCO_3 , $\mathcal{R} = 1.12$) plate with its optic axis oriented perpendicular to its entrance and exit faces. It is placed in linseed oil, which was chosen to match the index n_e of calcite. With the uniaxial plate we find the focus of an e-polarized beam is advanced by -3.4 mm, in good agreement with the predicted advance of $\Delta = -3.5$ mm (see Sec. S5: Polarization measurements for details on the o-polarized beam). Just as expected, both types of spaceplates advance the focus of a beam, just as if it had passed through an additional length of the background medium.

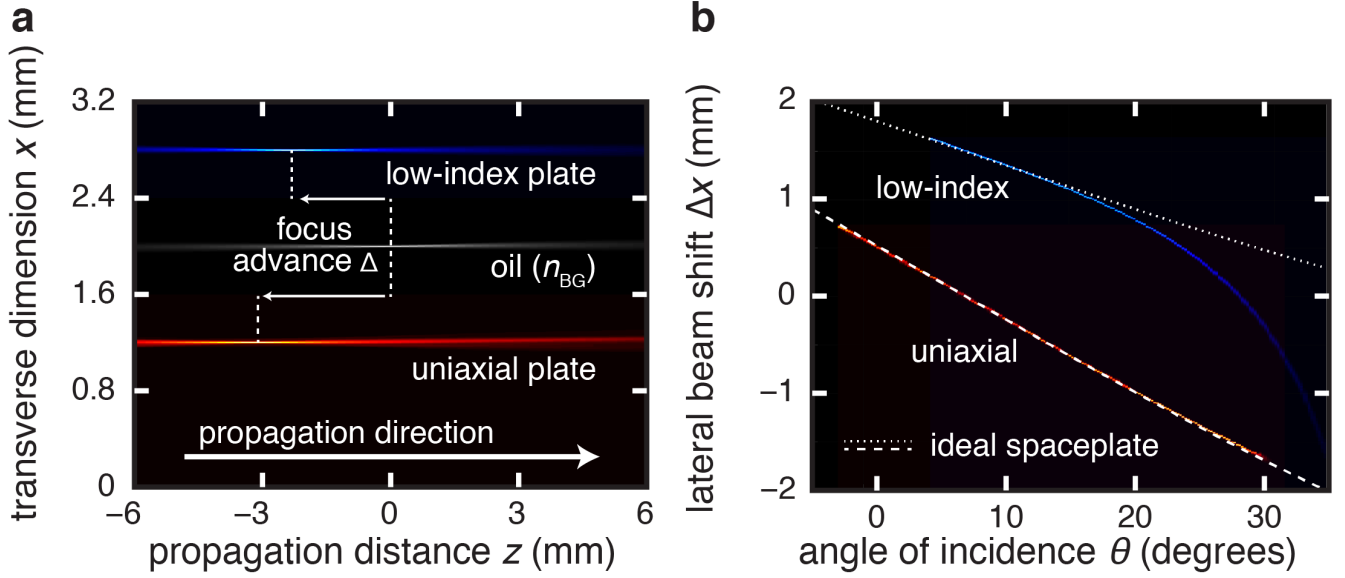


Fig. 2 | Experimental demonstration of space compression. For all plots, the false-colour along the plot-vertical gives the transverse intensity distribution along x at each z distance on the horizontal plot axis, with lighter colour corresponding to higher intensity. **a**, Focal shift, $\Delta = d - d_{\text{eff}}$. Middle data: Oil (grey). A converging beam comes to focus in oil at $z = 0$. Top data: Low-index spaceplate (blue). Propagation through a plate of air advances the focus position along z by $\Delta = -2.3$ mm. Bottom data: Uniaxial spaceplate (red). Propagation of an e-polarized beam through a calcite crystal with its fast axis along z advances the focus position by $\Delta = -3.4$ mm. The corresponding y intensity distributions are shown in Sec. S4 in the Supplementary Information, demonstrating a fully two-dimensional advance. **b**, The walk-off of a beam incident at an angle θ (low-index space plate, blue; uniaxial spaceplate, red). The dotted and dashed lines give the lateral beam shift for ideal spaceplates (*i.e.*, $\Delta x = -(\mathcal{R} - 1)d \sin \theta$) with the same thickness d and compression factor \mathcal{R} as the two spaceplates in **a**. Above a tilt of 15° , the low-index spaceplate starts to exhibit noticeable aberrations, deviating from the dotted line, due to the onset of total internal reflection and the failure of the small-angle approximation. By contrast, the uniaxial spaceplate acts as a perfect spaceplate for all measured tilt angles.

We now experimentally investigate the transverse beam displacement, an effect which is central to the action of the spaceplate. We vary the angle of incidence θ of the beam with respect to the spaceplate interface normal and record the beam's lateral displacement (indicated by Δx in Fig. 1a) upon exiting, shown in Fig. 2b. For both types of spaceplates, for small angles the observed displacement Δx (red and blue data) is equal to the ideal displacement of a beam travelling through d_{eff} of the linseed oil at

angle θ (dashed theory curves). However, for larger angles the displacement induced by the low-index plate deviates from that of an ideal spaceplate (see Sec. S6: [Transverse and lateral beam shifts due to a spaceplate](#)). In an imaging system, this discrepancy would act to introduce optical aberrations. This deviation is due to the failure of the small-angle approximation, most dramatically near the onset of total internal reflection at $\theta_{\text{crit}} = 42.5^\circ$. Aside from this aberration, total internal reflection imposes a severe limitation on the low-index spaceplate; as its refractive index n_{LI} decreases, its acceptance angle decreases as $\theta_{\text{crit}} = \arcsin(n_{\text{LI}}/n_{\text{BG}}) = \arcsin(1/\mathcal{R})$. Consequently, for the low-index spaceplate, the greater the compression factor \mathcal{R} is, the smaller the numerical aperture (NA, *i.e.*, θ_{crit}) will be. In contrast, the calcite crystal is found to perfectly reproduce the free space displacement for all measured angles. While both spaceplates act like a larger distance in oil for small angles, only the uniaxial spaceplate is exact and works out to large angles.

We now introduce a third type of spaceplate, a nonlocal metamaterial based on a multilayer stack, a structure made up of parallel flat layers of various media (Fig. 1i). Such a device would not depend on the bulk characteristics of naturally occurring media for performance and, hence, could potentially be engineered to possess much larger compression factors than those described above. With the layer normals along z , this class of structure satisfies the condition of translational invariance, like the homogeneous spaceplates. Again, the goal is to reproduce the transfer function H of a d_{eff} distance of free space in

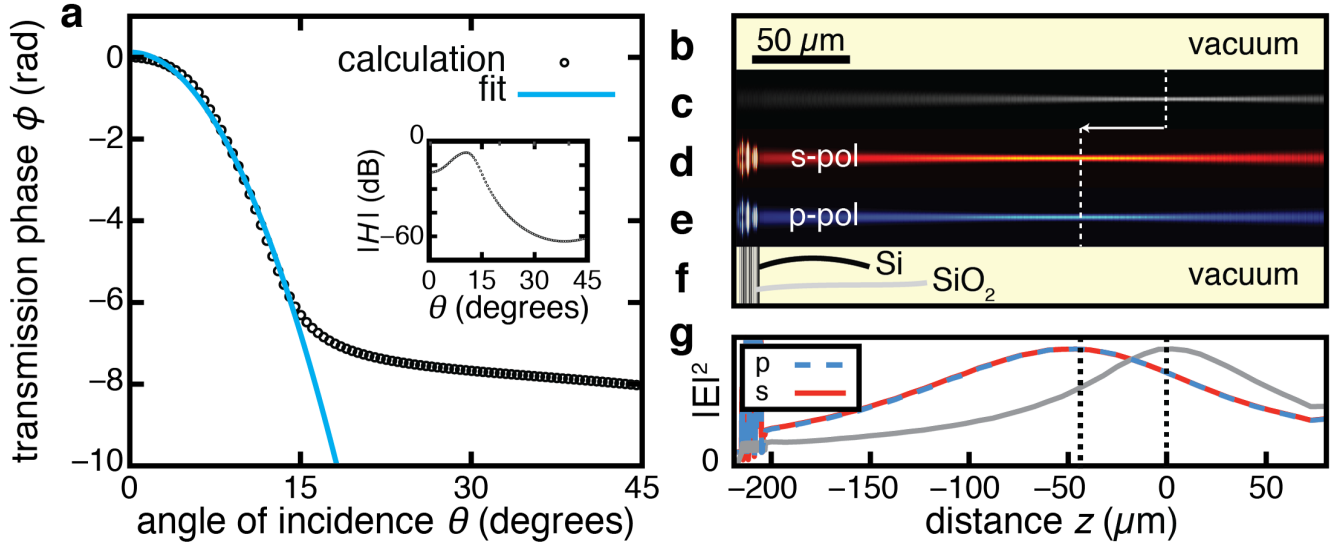


Fig. 3 | A nonlocal metamaterial spaceplate. **a**, A multilayer stack consisting of alternating layers of silicon and silica of various thicknesses is engineered to reproduce the Fourier transfer function H of vacuum for incident angles smaller than $\theta = 15^\circ$ at an optical wavelength of $\lambda = 1550$ nm. Plotted is the calculated transmission phase ϕ_{SP} of the metamaterial spaceplate (black circles) and a fitted vacuum transfer function phase ϕ_{BG} (blue curve). Here, we have subtracted a global phase of $\phi_G = -0.05$ rad. The fitted compression factor is $\mathcal{R} = 4.9$. The inset shows the transmission amplitude $|H|$. **b**, A full-wave simulation of the magnitude of the electric field $|E|^2$ of a focusing Gaussian beam (waist of 3λ , divergence of 6°) propagating in **c**, vacuum (grey), **d**, after propagating an s-polarized beam through the metamaterial (red, to scale), and **e**, after propagating a p-polarized beam through the metamaterial (blue, to scale). The corresponding structures (**b**, vacuum and **f**, spaceplate) are to scale. **g**, A cross section of $|E|^2$ along the beam axis. Transmission through the spaceplate advances the focus position along z by $\Delta = -43.2$ μm for both p-polarized (dashed blue) and s-polarized (solid red) light.

a structure of thickness d . We describe two design strategies for achieving this. One strategy is to create an effective negative uniaxial medium by alternating sub-wavelength thick layers between two materials³⁸. This would create a uniaxial spaceplate with the advantages that the birefringence (and, hence, \mathcal{R}) can be large and, also, slowly varied along z to avoid reflection at the interfaces. Instead, we primarily focus on a second strategy in which we search for novel multilayer structures using a genetic algorithm targeting ϕ_{BG} . The device this search yielded is composed of only two materials in a $d = 10.1752 \mu\text{m}$ -thick, 25-layer structure, and acts as a polarization-insensitive spaceplate with a compression factor of $\mathcal{R} = 4.9$ for vacuum-filled space, up to an incident angle of $\theta = 15^\circ$ (Fig. 3a). (See Sec. S7: [Spaceplate metamaterial](#) for more details on this structure.) Using full-wave simulations, we show that this structure indeed advances the focus of a converging beam in vacuum (Fig. 3b-c) towards the plate, as desired, by $\Delta = -43.2 \mu\text{m}$, which corresponds to a compression factor of $\mathcal{R} = 5.2$, in approximate agreement with the prediction. Crucially, unlike in the uniaxial or low-index spaceplates, the compression factor \mathcal{R} of this structure exceeds the ratio of any of the indices in the spaceplate ($n_{\text{Si}} \sim 3.48$, $n_{\text{SiO}_2} \sim 1.45$, $n_{\text{vac}} = 1$) and, thereby, demonstrates that this ratio does not impose a fundamental limit on \mathcal{R} . Remarkably, this device design is both polarization-insensitive and advances the focus for a bandwidth spanning 30 nm. (See Sec. S7: [Spaceplate metamaterial](#) for more details on the performance of this structure.) Both this design

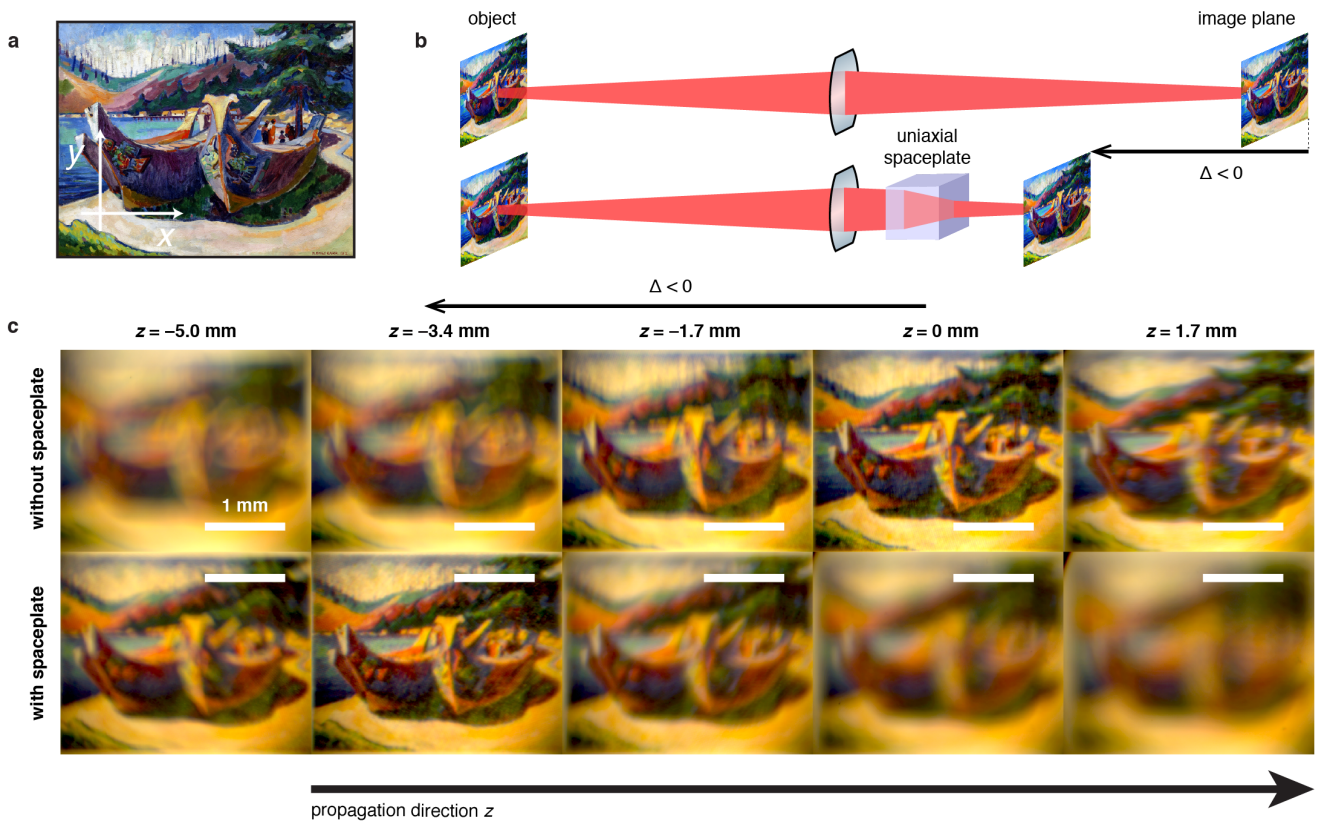


Fig. 4 | Advance of a broadband visible image using a spaceplate. **a**, This print of a painting was illuminated with incoherent white light. **b**, An image of the print is formed in either a background medium, glycerol, or through the calcite spaceplate in glycerol. **c**, Camera images at various distances z . The spaceplate advances the focal plane of the image by $\Delta = -3.4 \text{ mm}$ relative to the glycerol alone. The scale bar is the same length in all the images. This illustrates that the spaceplate does not change the magnification *i.e.*, the absence of any lens power. Note that the colour cast is due to the illumination.

and the effective-uniaxial design are relatively simple multilayer structures. This hints at the promise of more complicated multilayer stacks for creating spaceplates with large compression factors.

Finally, we use the uniaxial plate to experimentally demonstrate the reduction in size of a complete imaging system. A print of the painting in Fig. 4a is illuminated using an incoherent visible white-light source. A lens system forms an in-focus image of the print at an image plane inside a tank of glycerol placed after the last lens (Fig. 4b). Glycerol is used here due to its excellent transmission across the visible spectrum (See Methods). Figure 4c shows images captured by a CCD at a series of different positions z along the system axis (see Sec. ??). At $z = 0$, Fig. 4c shows that the captured image is in sharp focus, whereas at position $z = -3.4$ mm, the captured image is still out of focus, as it has not propagated far enough to fully form. We now look at how the spaceplate affects this image formation by placing the calcite crystal into the glycerol before the image plane. The bottom row of Fig. 4c shows the images captured at the same z positions as the top row, now with the spaceplate in place. Now, the image comes into focus sooner than with the glycerol alone. Specifically, the captured image is sharp at position $z = -3.4$ mm, whereas in the top row, the image is still forming. Thus, we observe an image advance of $\Delta = -3.4$ mm in approximate agreement with the theoretical prediction of $\Delta = -3.5$ mm. Furthermore, the magnification of the image is preserved, as evidenced by comparing the sizes of the images at their respective focal planes. Thus, the lens system has been shortened without changing the field of view, the NA, or the magnification. In contrast, shortening the lens system by reducing the lens focal lengths would change all three of these important imaging system parameters. Finally, the entire color image remains in focus simultaneously, illustrating the broadband operation of the uniaxial spaceplate.

Multiple methods could be employed to improve the performance of the demonstrated spaceplates. The low-index and uniaxial designs can be combined (*i.e.*, $n_{LI} = n_e < n_{BG}$) to doubly enhance the compression $\mathcal{R} = \frac{n_o}{n_e} \frac{n_{BG}}{n_e}$. In recent years, much attention has been given to engineering optical media with refractive indices below unity^{34,39,40}, which would enable a low-index spaceplate for vacuum. However, replacing *vacuum* is not always desirable, which relaxes this challenging requirement. In particular, replacing higher-index background-media would enable a higher system NA. While high-index background-media is problematic for regular (*i.e.*, refractive) lenses, it is not for zone plates and metalenses. As needed for the uniaxial spaceplate with a large \mathcal{R} , strongly anisotropic responses are routinely produced using thin-film stacks and metamaterials^{41–44}. Even larger birefringence, and thus compression factor, can be produced by incorporating low-index materials in these stacks⁴⁵. Using dynamic birefringent materials (*e.g.*, liquid crystals⁴⁴), one could develop devices of variable \mathcal{R} as would be required for, say, a variable-focus lens system.

From a broader perspective, the spaceplate demonstrates the power of an optical element that operates directly on the phase of transverse Fourier components of a light field. Past work has instead controlled the transmittance of such Fourier components (the so-called ‘nonlocal’ response, *e.g.*,^{8–10}). This transmittance control was used to demonstrate a broadband angular pass-filter⁴⁶ and analog optical computations, such as derivatives and spatial imaging filters^{47–49}. Combining transmittance and phase control would enable all of the benefits of Fourier optics (*e.g.*, spatial filtering) without needing a lens system (*e.g.*, a 4f) to access the farfield. In turn, repeatedly iterating between this momentum-dependent Fourier control and position-dependent control has been shown to enable fully arbitrary spatial transformations of light fields⁵⁰. Using multilayer metamaterials and metasurfaces to respectively accomplish these two controls opens the possibility of complete spatial control of light in a monolithic device.

References

1. Hooke, R. *Micrographia: or, Some physiological descriptions of minute bodies made by magnifying glasses* (J. Martyn and J. Allestry, London, 1665), first edn.
2. Khorasaninejad, M. & Capasso, F. Metalenses: Versatile multifunctional photonic components. *Science* **358**, eaam8100 (2017).
3. Yu, N. *et al.* Light Propagation with Phase Discontinuities: Generalized Laws of Reflection and Refraction. *Science* **334**, 333–337 (2011).
4. Kildishev, A. V., Boltasseva, A. & Shalaev, V. M. Planar photonics with metasurfaces. *Science* **339**, 1232009 (2013).
5. Yu, N. & Capasso, F. Flat optics with designer metasurfaces. *Nature Materials* **13**, 139–150 (2014).
6. Meinzer, N., Barnes, W. L. & Hooper, I. R. Plasmonic meta-atoms and metasurfaces. *Nature Photonics* **8**, 889–898 (2014).
7. Chen, H.-T., Taylor, A. J. & Yu, N. A review of metasurfaces: physics and applications. *Reports on Progress in Physics* **79**, 076401 (2016).
8. Castaldi, G., Galdi, V., Alù, A. & Engheta, N. Nonlocal transformation optics. *Physical Review Letters* **108**, 063902 (2012).
9. Silva, A. *et al.* Performing Mathematical Operations with Metamaterials. *Science* **343**, 160–163 (2014).
10. Kwon, H., Sounas, D., Cordaro, A., Polman, A. & Alù, A. Nonlocal Metasurfaces for Optical Signal Processing. *Physical Review Letters* **121**, 173004 (2018).
11. Goodman, J. W. *Fourier Optics* (Roberts & Company, Englewood, Colorado, 2005), third edn.
12. Winston, R. Principles of solar concentrators of a novel design. *Solar Energy* **16**, 89–95 (1974).
13. Halir, R. *et al.* Ultra-broadband nanophotonic beamsplitter using an anisotropic sub-wavelength metamaterial. *Laser and Photonics Reviews* **10**, 1039–1046 (2016).
14. Czerny, M. & Turner, A. F. Über den astigmatismus bei spiegelspektrometern. *Zeitschrift für Physik* **61**, 792–797 (1930).
15. Genevet, P., Capasso, F., Aieta, F., Khorasaninejad, M. & Devlin, R. Recent advances in planar optics: from plasmonic to dielectric metasurfaces. *Optica* **4**, 139–152 (2017).
16. Cui, Y., Kang, L., Lan, S., Rodrigues, S. & Cai, W. Giant chiral optical response from a twisted-arc metamaterial. *Nano Letters* **14**, 1021–1025 (2014).
17. Karimi, E. *et al.* Generating optical orbital angular momentum at visible wavelengths using a plasmonic metasurface. *Light: Science & Applications* **3**, e167 (2014).
18. Ni, X., Wong, Z. J., Mrejen, M., Wang, Y. & Zhang, X. An ultrathin invisibility skin cloak for visible light. *Science* **349**, 1310–1314 (2015).
19. Arbabi, A., Arbabi, E., Horie, Y., Kamali, S. M. & Faraon, A. Planar metasurface retroreflector. *Nature Photonics* **11**, 415–420 (2017).
20. Faraji-Dana, M. *et al.* Compact folded metasurface spectrometer. *Nature Communications* **9**, 4196 (2018).

21. Yang, Y. *et al.* Nonlinear Fano-Resonant Dielectric Metasurfaces. *Nano Letters* **15**, 7388–7393 (2015).
22. Li, G. *et al.* Continuous control of the nonlinearity phase for harmonic generations. *Nature Materials* **14**, 607–612 (2015).
23. Li, G., Zhang, S. & Zentgraf, T. Nonlinear photonic metasurfaces. *Nature Reviews Materials* **2**, 17010 (2017).
24. Chen, W. T. *et al.* A broadband achromatic metalens for focusing and imaging in the visible. *Nature Nanotechnology* **13**, 220–226 (2018).
25. Zhou, W. *et al.* Lasing action in strongly coupled plasmonic nanocavity arrays. *Nature Nanotechnology* **8**, 506–511 (2013).
26. Xu, L. *et al.* Metasurface quantum-cascade laser with electrically switchable polarization. *Optica* **4**, 468–475 (2017).
27. Rubin, N. A. *et al.* Matrix Fourier optics enables a compact full-Stokes polarization camera. *Science* **365**, eaax1839 (2019).
28. Ni, X., Kildishev, A. V. & Shalaev, V. M. Metasurface holograms for visible light. *Nature Communications* **4**, 2807 (2013).
29. Banerji, S. *et al.* Imaging with flat optics: metalenses or diffractive lenses? *Optica* **6**, 805–810 (2019).
30. Armstrong, S. *et al.* Programmable multimode quantum networks. *Nature Communications* **3**, 1026 (2012).
31. Fresnel, A.-J. *Oeuvres complètes d’Augustin Fresnel*. Nineteenth Century Collections Online (NCCO): Science, Technology, and Medicine: 1780-1925 (Imprimerie Impériale, Paris).
32. Miyamoto, K. The phase Fresnel lens. *Journal of the Optical Society of America* **51**, 17–20 (1961).
33. Hobbs, P. C. D. *Building electro-optical systems: Making it all work* (John Wiley & Sons, Inc., Hoboken, NJ, USA, 2009), second edn.
34. Vulis, D. I., Reshef, O., Camayd-Muñoz, P. & Mazur, E. Manipulating the flow of light using Dirac-cone zero-index metamaterials. *Reports on Progress in Physics* **82**, 012001 (2019).
35. Leonhardt, U. Optical conformal mapping. *Science* **312**, 1777–1780 (2006).
36. Pendry, J. B., Schuring, D. & Smith, D. R. Controlling electromagnetic fields. *Science* **312**, 1780–1782 (2006).
37. Roberts, D. A., Kundtz, N. & Smith, D. R. Optical lens compression via transformation optics. *Optics Express* **17**, 16535–16542 (2009).
38. Cai, W. & Shalaev, V. *Optical Metamaterials* (Springer New York, New York, NY, 2010).
39. Valentine, J. *et al.* Three-dimensional optical metamaterial with a negative refractive index. *Nature* **455**, 376–379 (2008).
40. Liberal, I. & Engheta, N. The rise of near-zero-index technologies. *Science* **358**, 1540–1541 (2017).
41. Poddubny, A., Iorsh, I., Belov, P. & Kivshar, Y. Hyperbolic metamaterials. *Nature Photonics* **7**, 958–967 (2013).
42. Popov, V., Lavrinenko, A. V. & Novitsky, A. Operator approach to effective medium theory to overcome a breakdown of Maxwell Garnett approximation. *Physical Review B* **94**, 085428 (2016).

43. Niu, S. *et al.* Giant optical anisotropy in a quasi-one-dimensional crystal. *Nature Photonics* **12**, 392–396 (2018).
44. Wei, B. Y. *et al.* Generating switchable and reconfigurable optical vortices via photopatterning of liquid crystals. *Advanced Materials* **26**, 1590–1595 (2014).
45. Ji, W., Luo, J. & Lai, Y. Extremely anisotropic epsilon-near-zero media in waveguide metamaterials. *Optics Express* **27**, 19463–19473 (2019).
46. Shen, Y. *et al.* Optical broadband angular selectivity. *Science* **343**, 1499–1501 (2014).
47. Zhou, Y., Zheng, H., Kravchenko, I. I. & Valentine, J. Image Processing Based on Compound Flat Optics. *arXiv:1909.02132* (2019).
48. Zhang, Y., Zheng, J., Wang, Y., Zhao, J. & Ruan, S. Design and fabrication of multilayer dielectric film for combination device spatial filter. *Optik* **181**, 528–537 (2019).
49. Dong, Z., Si, J., Yu, X. & Deng, X. Optical spatial differentiator based on subwavelength high-contrast gratings. *Applied Physics Letters* **112**, 181102 (2018).
50. Morizur, J.-F. *et al.* Programmable unitary spatial mode manipulation. *Journal of the Optical Society of America A* **27**, 2524–2531 (2010).
51. Entezar, S. R. & Habi, M. K. Refraction and reflection from the interface of anisotropic materials. *Physica Scripta* **94**, 085502 (2019).

Acknowledgements The authors acknowledge support from the Transformative Quantum Technologies program of the Canada First Research Excellence Fund, the Canada Research Chairs Program, and the Natural Sciences and Engineering Research Council of Canada. AA was supported by Mitacs Globalink. OR acknowledges the support of the Banting Postdoctoral Fellowship of NSERC. We thank Eric Mazur for suggesting the use of glycerol.

Author Contributions OR, JL, and RB conceived the basic idea for this work. JL did the theory work. OR, KB, AA, JL, and LG designed the experiment. MD and OR carried out the measurements. OR analysed the experimental results. OR, AA, and JL did the multilayer design. OR performed the full-wave simulations. JL and RB supervised the research and the development of the manuscript. OR wrote the first draft of the manuscript, and all authors subsequently took part in the revision process and approved the final copy of the manuscript.

Methods

Homogeneous spaceplates

Background media: The background medium for measurements in Fig. 2 is linseed oil (also known as flaxseed oil). This oil (refractive index $n_{BG} = 1.4795$ at an optical wavelength of $\lambda = 532$ nm) was chosen to match to n_e of the uniaxial spaceplate material ($n_e = 1.486$). The colour imaging measurements in Fig. 4 instead used a background medium of glycerol ($n_{BG} = 1.4743$ at 532 nm). While glycerol matches n_e slightly worse than linseed oil, it has a higher transmittivity across the visible spectrum, which makes it appropriate for full-colour imaging.

Uniaxial spaceplate: We use a 20.04 mm \times 19.98 mm \times 29.84 mm (width \times height \times depth, ± 0.06 mm) right rectangular prism made of calcite that was cut with its extraordinary optical axis along the depth direction. The surfaces perpendicular to this axis are polished and used as the entrance and exit faces.

Note that the surface quality is low, which somewhat distorts and scatters the beam in the measurements in Fig. 2 (see Sec. S3: [Fabricated spaceplates](#)). Calcite is negative uniaxial with refractive indices $n_e = 1.486$, $n_o = 1.660$ at a wavelength of $\lambda = 532$ nm. For e-polarized light in a background medium with $n_{BG} = n_e$, this crystal gives an expected enhancement factor of $\mathcal{R} = n_o/n_e = 1.117$ and an advance $\Delta = (1 - \mathcal{R})d = -3.494$ mm (*i.e.*, a shift towards the crystal). The o-polarized light will experience a medium of isotropic refractive index n_o . Consequently, $R = n_{BG}/n_o = 0.895$ and $\Delta = (1 - \mathcal{R})d = 3.126$ mm.

Low-index spaceplate: Our implementation of a low-index spaceplate consists of a glass-faced cylindrical cell containing air (length $d = 4.37 \pm 0.06$ mm and diameter $= 25.82 \pm 0.06$ mm). The faces are 0.14 ± 0.01 mm thick microscope coverglass pieces (see Sec. S3: [Fabricated spaceplates](#)).

Experimental setup

Light sources: The measurements in Fig. 2 used a 4.5 mW diode laser with an optical wavelength of 532 nm. We spatially filter the laser beam with a single-mode fiber. The beam that is then focused to a waist of $\omega_0 = 9.5 \pm 0.5$ μm (e^{-2} radius) with a $0.69^\circ \pm 0.03^\circ$ e^{-2} half-angle and a Rayleigh range of 0.79 ± 0.08 mm, all in the background oil medium. The measurements in Fig. 4 instead used incoherent visible white-light illumination.

Field relay system: The light field inside the oil background medium is relayed to outside the oil using two lenses (focal lengths, $f_1 = 100$ mm and $f_2 = 200$ mm arranged in a 4f geometry) resulting in a magnification $M = f_2/f_1 = 2$. We use a camera to record this relayed light-field. For the measurements in Fig. 2, we use a monochromatic camera (3088×2076 pixels, $2.4 \mu\text{m} \times 2.4 \mu\text{m}$ each, 12 bit). For the measurements in Fig. 4, we use a colour camera (1936×1216 pixels, $5.86 \mu\text{m} \times 5.86 \mu\text{m}$ each, 12 bit). In the figures, we report the dimensions of the field inside the oil. The ratio of transverse distance after the relay to in the oil is M . The same ratio but for distance along z is M^2/n_{BG} .

Spaceplate measurements: For the measurements in Figs. 2a and 4, we move the camera along z , recording an image at steps of 0.02 in (0.508 mm) over a range of 60 and 100 mm, respectively. For the measurements in Fig. 2b, the camera z -position is set so that the camera images the beam focus. In order to measure the lateral beam displacement Δx , the spaceplate is then tilted by an angle θ about y in steps of 0.25° over a range of 40° and 43.5° for the calcite and air plates, respectively (note that these ranges are the maximum allowed by the clear aperture of the respective spaceplate). For each camera position z or crystal angle θ , the recorded image is summed along the y -direction to arrive at an intensity distribution along x . These x intensity distributions are presented along the vertical direction of the plots in Fig. 2.

Polarization control: A uniaxial spaceplate acts to replace space for e-polarized light. However, the e-polarization direction varies depending on the angle of the incident wavevector relative to the crystal's extraordinary optic axis. In order for the incident light field to be simultaneously e-polarized and approximately uniformly polarized along one direction, the crystal is tilted slightly about y by an angle α relative to the incident beam (and system axis). The tilt is $\alpha = 4.5^\circ$ for Fig. 2a and $\alpha = 8^\circ$ for Fig. 4. An x -polarized light field will then be e-polarized with respect to the crystal; a y -polarized field will be o-polarized. For the laser, the incident polarization is set by a polarizing beamsplitter followed by waveplates. The polarization of the white light is set by a film polarizer designed for broadband visible light. More generally, the uniaxial spaceplate works for a lightfield with an angularly non-uniform polarization that is extraordinary everywhere (*e.g.*, a radially polarized field).

Coordinate system: We use $x \times y \times z$ as a coordinate system for the experiment, where x and y are the transverse directions and z is the optical system axis (*i.e.*, the beam axis). The crystal's height dimension is along y . The extraordinary optical axis of the tilted crystal defines z' of a second coordinate system, $x' \times y \times z'$. Thus, the second coordinate system is related to the first by a rotation about y by angle α .

The uniaxial spaceplate always acts as $d_{\text{eff}} = \mathcal{R}d$ distance along z' with $\mathcal{R} = n_o/n_e$. This tilt reduces the effective distance along z by a factor $\cos \alpha$, which for small α is approximately unity.

Colour imaging: For the measurements in Fig. 4, we image a print on paper ($x \times y$ dimensions, 15 mm \times 12 mm) of a painting (*First Nations War Canoes in Alert Bay* by Emily Carr, 1912). A two-lens system (NA= 0.025) creates an image of the print in the oil with magnification 0.209 ± 0.001 . This image is then relayed out of the oil as described above. In the focused image plane, the image has $x \times y$ dimensions of 6.25 mm \times 5.03 mm on the camera sensor.

Multilayer metamaterial spaceplate

Metamaterial structure: We consider structures made up of planar layers alternating between two materials, silicon and silica (*i.e.*, a ‘multilayer stack’). Each layer can have an arbitrary thickness larger than 10 nm, set by feasible fabrication capabilities. The combined thickness of the entire stack is designed to be approximately 10 μm .

Genetic algorithm: Our aim is to design a multilayer stack to replace a background medium of vacuum. To do so, we search for a structure that gives a phase profile ϕ_{SP} that matches the phase profile $\phi_{\text{BG}}(d_{\text{eff}})$ resulting from propagation through a slab of vacuum of length d_{eff} . We restrict this aim to a range of incident angle from zero to θ_{max} (*i.e.*, the NA of the spaceplate). The search is conducted with a genetic algorithm whose goals are to maximize d_{eff} while minimizing any optical aberration resulting from a non-ideal phase profile. To quantify the latter goal, we first calculate the difference of the slope from that of the ideal profile, $\Delta\phi' = \phi'_{\text{SP}} - \phi'_{\text{BG}}$, where $\phi' = \partial\phi/\partial\theta$. This angular slope is the relevant quantity to consider since any global phase ϕ_G and phase wraps $2\pi m$ will be eliminated by the derivative. We then find the root-mean-square (RMS) of this difference, $\Delta\phi'_{\text{RMS}}$. The RMS deviation $\Delta\phi'_{\text{RMS}}$ is an optical aberration that results in an increased beam waist $\omega_{\text{SP}} = \omega_0(1 + \theta_{\text{max}}\Delta\phi'_{\text{RMS}})$ relative to the waist $\omega_0 = \lambda/(\pi\theta_{\text{max}})$ in the absence of the multilayer stack. As a worst case scenario, this larger waist will increase the Rayleigh range to $z_{\text{SP}} = \pi\omega_{\text{SP}}^2/\lambda$. The parameter z_{SP} increases with aberration and the inverse of the usable angle θ_{max}^{-1} . The two goals of the algorithm can be combined in a single fitness function, $F = d_{\text{eff}}/z_{\text{SP}} = \pi d_{\text{eff}}\theta_{\text{max}}^2/(\lambda(1 + \theta_{\text{max}}\Delta\phi'_{\text{RMS}})^2)$, where we have used the small-angle approximation repeatedly. The larger the value of F is, the better the performance of the multilayer spaceplate will be.

We now outline the functioning of the genetic algorithm. Each generation in the genetic algorithm had a population size of 500. The DNA of each population member was the material and the thickness of each layer in the stack. We used two materials, silica and silicon. The maximum number of layers was set to 40 and each layer was constrained to have a thickness greater than 10 nm. For each member, we use the standard transfer matrix formalism to calculate the complex transmission amplitude $H = |H|\exp(i\phi_{\text{SP}})$ of the multilayer stack for a set of incident angles θ . We use nonlinear regression to fit ϕ_{SP} with an ideal phase profile $\phi_{\text{BG}}(d_{\text{eff}})$, giving d_{eff} and, with this fit, we numerically calculate ϕ'_{RMS} . Both the fit and calculation are conducted over a range of input angles from zero to $\theta_{\text{max}} = 15^\circ$. With these performance parameters we find the fitness F of each population member. The device thickness of the first generation is constrained to 10 μm , but this parameter is not constrained for later generations. The algorithm was carried out until there was a convergence in the fitness of the “best” member of each generation. For the structure reported here, this took 4000 generations.

Full-wave simulations: The simulation in Fig. 3 was performed using a commercial 2D finite-difference time-domain solver. The boundary conditions are perfectly-matched layers. Exact details about the geometry of the structure and material parameters can be found in Sec. S7: [Spaceplate metamaterial](#).

Supplementary Materials

Below are the supplementary materials for *Towards ultra-thin imaging systems: an optic that replaces space* by Orad Reshef, Michael P. DelMastro, Katherine K. M. Bearne, Ali H. Alhulaymi, Lambert Giner, Robert W. Boyd, and Jeff S. Lundeen. In Sec. S1, we have diagrams and descriptions of our experimental setups. In Sec. S2, we derive the refractive index for an anisotropic homogeneous spaceplate medium. We then step through the different types of solutions that are yielded by this derivation and their properties. In Sec. S3, we describe the fabricated spaceplates we use in our measurements. In Sec. S4, we present additional beam-focus measurements as proof of the two-dimensional action of the spaceplate. In Sec. S5, we describe ordinarily and extraordinarily polarized beam measurements conducted with the uniaxial spaceplate. In Sec. S6, we derive the lateral shift Δx . Section S7 summarizes details about the nonlocal metamaterial spaceplate structure.

S1 Experimental setup

The experimental setup is shown in (Fig. S1). In the following, we detail the arrangement of lenses.

S1.1 Field relay system

Both the beam measurements and imaging measurements use a field relay lens system to relay the full $E_{BG}(x, y, z)$ electric field profile to a region outside the tank containing the background medium and spaceplate. The $f_1 = 100$ mm lens after the tank and the $f_2 = 200$ mm lens are separated by a distance $s_{4F2} = 300$ mm, which constitutes a common lens system known as a 4f system. The system relays the field outside $E_{out}(x, y, z)$ such that $E_{out}(Mx, My, M^2z/n_{BG}) \propto E_{BG}(x, y, z)$. Outside the tank, we use an image sensor (CCD) to record the intensity spatial-distribution in the x, y plane. We then scan the CCD along z . Five images are taken at each step and averaged to reduce camera noise. A shutter is closed in order to acquire background images, which are subtracted from the raw images to compensate for stray light and camera noise.

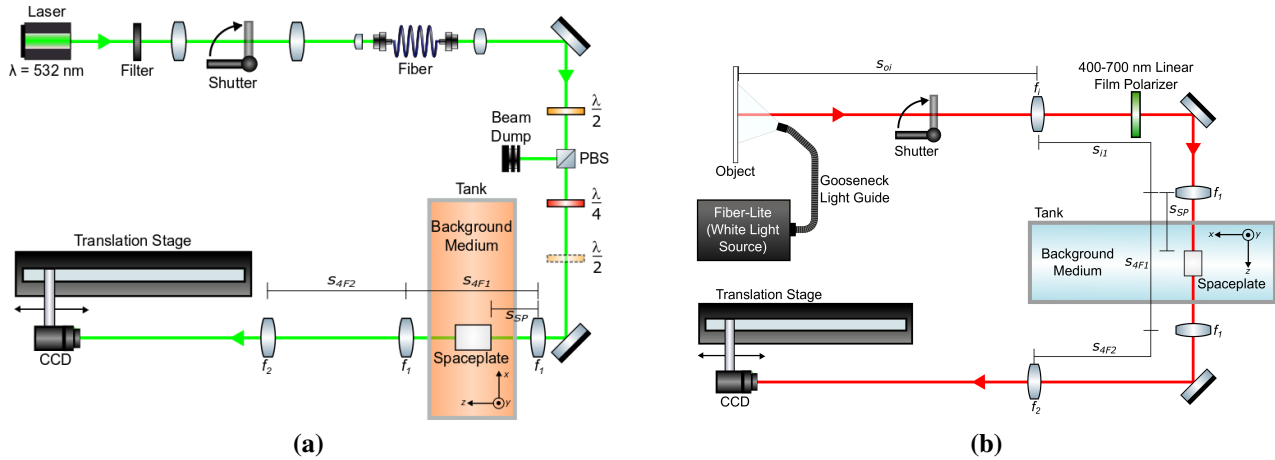


Fig. S1 | Experimental setup to measure the action of a spaceplate. See the text for details. **a**, We focus a beam through a spaceplate and measure its shift in z and x . **b**, We perform full colour imaging through a spaceplate.

S1.2 Beam measurements

The beam measurement setup is shown in Fig. S1a. A diode laser produces a beam of wavelength 532 nm with a power of 4.5 mW. This beam is attenuated using a filter and then has its spatial mode filtered by a single-mode fiber. The beam exiting the fiber is collimated. A half-waveplate ($\lambda/2$) and polarizing beamsplitter (PBS) are used to vary the beam intensity and polarize the beam. The beam's polarization is subsequently controlled by a zero-order half-waveplate ($\lambda/2$) and quarter-waveplate ($\lambda/4$). The lens before the tank, $f_1 = 100$ mm, is used to focus the beam through the spaceplate. The spaceplate's entrance surface is located 80 mm from this f_1 lens. The tank contains linseed oil as a background medium. We then use the field relay system to image the transmitted beam.

S1.3 Imaging measurements

The imaging measurement setup is shown in Fig. S1b. With visible white light, we illuminate a print of a painting printed on ordinary white paper. At a distance $s_{oi} = 475$ mm from the print is a lens of focal length $f_i = 500$ mm. A further $s_{i1} = 355$ mm from the f_i lens is the first $f_1 = 100$ mm lens. Together this lens pair collects the light reflected from the print, transmits the light through the spaceplate in the tank, which then forms in the background medium an image of the print. Between this lens pair is a linear film polarizer (visible broadband, 400 – 700 nm), which we rotate to set the polarization of the light. The spaceplate is placed $s_{sp} \approx 80$ mm after this f_1 lens. The background medium in the tank is now glycerol rather than linseed oil since the former has a high transmission across the visible spectrum, which is ideal for full-colour imaging. We then use the field relay system to image the field after the spaceplate at various propagation distances z .

S2 Homogeneous spaceplate solutions

S2.1 General solution for an angle-dependent refractive index

The goal of a spaceplate is to transform an incoming light-field in an identical manner (for the purposes of imaging) to propagation through a slab of an isotropic homogeneous medium. To do so, the spaceplate must multiply the complex amplitude of each plane-wave in an incoming field by the function, $\exp(i\phi_{BG})$. In particular, a spaceplate of thickness d must impart a phase ϕ_{SP} that is equal to the phase ϕ_{BG} due to the propagation through distance d_{eff} of the medium. Both d and d_{eff} are along what we set to be the z -axis.

In more detail, in a medium of index n_{BG} , a plane-wave has phase difference, $\phi_{BG} = \vec{k}^{(BG)} \cdot \vec{r}$, between two positions separated by vector $\vec{r} = (x, y, z = d_{eff})$, where $\vec{k}^{(BG)} = (k_x^{(BG)}, k_y^{(BG)}, k_z^{(BG)})$ is the wavevector. Here, $|\vec{k}^{(BG)}| = n_{BG}k_0 \equiv k_{BG}$ is the wavenumber in the medium and $k_0 = 2\pi/\lambda$ is the vacuum wavenumber. Inside the spaceplate, the wavevector is $\vec{k}^{(SP)} = (k_x^{(SP)}, k_y^{(SP)}, k_z^{(SP)})$. If we consider spaceplates made up of plates or layers whose interfaces are x, y planes, then $k_x^{(SP)} = k_x^{(BG)}$ and $k_y^{(SP)} = k_y^{(BG)}$ due to momentum conservation. Consequently, such a spaceplate will automatically reproduce the contribution to the phase due to displacement in \vec{r} by x and y , i.e., $\phi_{SP} = k_x^{(SP)}x + k_y^{(SP)}y + k_z^{(SP)}d = k_x^{(BG)}x + k_y^{(BG)}y + k_z^{(SP)}d$. The remaining component to be reproduced is the phase due to the displacement along z in the medium, $\phi_{BG} = k_z^{(BG)}d_{eff}$. In a homogeneous spaceplate this phase is $\phi_{SP} = k_z^{(SP)}d$. With this definition, the goal reduces to making the Fourier transfer function for propagation, $H = \exp(i\phi)$, equal for the spaceplate and the medium up to a global offset phase ϕ_G :

$$\begin{aligned} e^{i\phi_{SP}} &= e^{i\phi_{BG} + i\phi_G} \\ \implies 2\pi m &= \phi_{SP} - \phi_{BG} - \phi_G \end{aligned} \tag{S1}$$

$$2\pi m = k_z^{(SP)}d - k_z^{(BG)}d_{eff} - \phi_G, \tag{S2}$$

where m is an integer.

If the plane-wave is traveling in the medium at an angle θ to the z -axis, we can express the z -component of the wavevector as

$$k_z^{(\text{BG})} = k_{\text{BG}} \cos \theta. \quad (\text{S3})$$

In order to match this $\cos \theta$ variation, the spaceplate must produce an angle-dependent phase. To produce this dependence, one possible scenario is a spaceplate made of a non-isotropic material. That is, we consider a spaceplate material with a refractive index $n(\theta_{\text{SP}})$ that varies with the wavevector angle inside the spaceplate θ_{SP} , such that the wavenumber would be $k_{\text{SP}} = n(\theta_{\text{SP}})k_0$. In this case, the z -component of the wavevector is

$$k_z^{(\text{SP})} = n(\theta_{\text{SP}})k_0 \cos \theta_{\text{SP}} = \tilde{n}k_{\text{BG}} \cos \theta_{\text{SP}}, \quad (\text{S4})$$

where we defined the refractive index ratio, $\tilde{n} = \tilde{n}(\theta_{\text{SP}}) \equiv n(\theta_{\text{SP}})/n_{\text{BG}}$. Since transverse momentum is conserved throughout, we define it as a single parameter $k_{\perp} \equiv \sqrt{(k_x^{(\text{SP})})^2 + (k_y^{(\text{SP})})^2} = \sqrt{(k_x^{(\text{BG})})^2 + (k_y^{(\text{BG})})^2}$.

In particular, by the Pythagorean theorem, $k_{\perp}^2 = k_{\text{SP}}^2 - (k_z^{(\text{SP})})^2$ and, also,

$$\begin{aligned} k_z^{(\text{BG})} &= \sqrt{k_{\text{BG}}^2 - k_{\perp}^2} \\ &= \sqrt{k_{\text{BG}}^2 - \left(k_{\text{SP}}^2 - (k_z^{(\text{SP})})^2\right)} \\ &= \sqrt{k_{\text{BG}}^2 - \tilde{n}^2 k_{\text{BG}}^2 (1 - \cos^2 \theta_{\text{SP}})} \\ &= k_{\text{BG}} \sqrt{1 - \tilde{n}^2 \sin^2 \theta_{\text{SP}}}. \end{aligned} \quad (\text{S5})$$

The goal of these manipulations was to ensure that the only angle that appears in the expressions for both wavevectors is θ_{SP} . Note that these relations inherently account for refraction at the interfaces.

We insert the two wavevector equations, Eq. (S4) and Eq. (S5), into the phase condition in Eq. (S1) to obtain,

$$2\pi m = k_{\text{BG}} d \tilde{n} \cos \theta_{\text{SP}} - k_{\text{BG}} d_{\text{eff}} \sqrt{1 - \tilde{n}^2 \sin^2 \theta_{\text{SP}}} - \phi_{\text{G}}. \quad (\text{S6})$$

We can rearrange this equation to isolate the phase offsets in a single parameter,

$$C \equiv \left(m + \frac{\phi_{\text{G}}}{2\pi}\right) \frac{\lambda}{n_{\text{BG}} d} = \tilde{n} \cos \theta_{\text{SP}} - \frac{d_{\text{eff}}}{d} \sqrt{1 - \tilde{n}^2 \sin^2 \theta_{\text{SP}}}. \quad (\text{S7})$$

We then solve for \tilde{n} and recall the definition of $\mathcal{R} = d_{\text{eff}}/d$ to yield Eq. (1) in the main text, the general equation that describes the index of refraction for a homogeneous spaceplate,

$$\tilde{n}(\theta_{\text{SP}}) = \frac{n(\theta_{\text{SP}})}{n_{\text{BG}}} = \frac{C \pm \sqrt{C^2 + (\mathcal{R}^2 - C^2)(1 + \mathcal{R}^2 \tan^2 \theta_{\text{SP}})}}{(1 + \mathcal{R}^2 \tan^2 \theta_{\text{SP}}) \cos \theta_{\text{SP}}}. \quad (\text{S8})$$

The physical meaning of C can be understood by re-expressing it as

$$C(\theta_{\text{SP}}) = \frac{2\pi m(\theta_{\text{SP}}) + \phi_{\text{G}}}{k_{\text{BG}} d}, \quad (\text{S9})$$

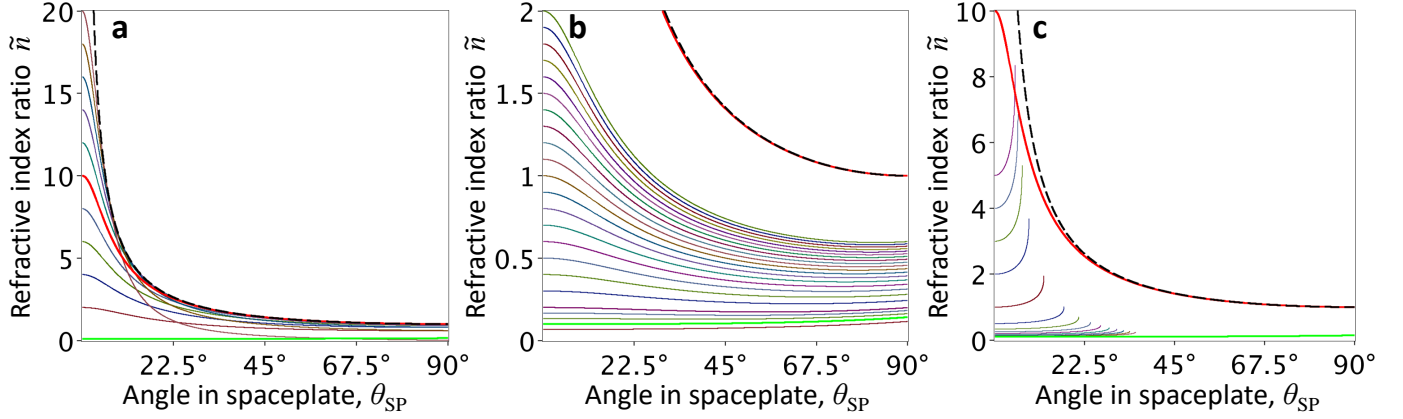


Fig. S2 | General angle-dependent refractive index solutions for a spaceplate. Plotted is the index ratio, $\tilde{n} \equiv n(\theta_{\text{SP}})/n_{\text{BG}}$. In the three panels, all the solutions are for $\mathcal{R} = 10$, the black dashed line is the bound on all solutions (Eq. (S13)), the red line corresponds to a uniaxial spaceplate ($C = 0$, Eq. (S12)), and the green line corresponds to the solution approximated by the low-index spaceplate ($C = 1/\mathcal{R} - \mathcal{R}$). **a**, Positive root solutions for $-\mathcal{R} \leq C \leq \mathcal{R}$, *i.e.*, $C = \mathcal{R}(j/5 - 1)$ for $j = 0$ to 20 . **b**, Positive root solutions for $C = j/\mathcal{R} - \mathcal{R}$ with $j = 1$ to 10 and $3j = 2$ to 6 . **c**, Negative root solutions for $C = \mathcal{R} + j$ with $j = 1$ to 5 and $1/j = 1$ to 10 . For every positive-valued refractive index solution \tilde{n}_+ , there is a mirror negative-valued solution, $\tilde{n}_- = -\tilde{n}_+$.

where we have made the potential dependence of the integer m on angle explicit. C is the ratio of the total phase offset to the phase ϕ_{BG} accumulated by a wave at angle $\theta_{\text{SP}} = \theta = 0$, traveling distance d .

An infinite family of solutions are parametrized by Eq. (S8). First, there are two branches to the solution corresponding to the positive and negative roots and, second, C is arbitrary. In the following subsections, we describe some of these solutions.

S2.1.1 Low-index spaceplate

We start with the positive-root solution. In the family defined by $C > (1 - \mathcal{R})$, $n(\theta_{\text{SP}})$ is globally smaller than the refractive index of the background medium, *i.e.*, $n(\theta_{\text{SP}}) < n_{\text{BG}}$. The special case where $C = 1/\mathcal{R} - \mathcal{R}$ exhibits the lowest curvature at $\theta_{\text{SP}} = 0$ in this family. In other words, it is the flattest solution for small angles and, thus, has the lowest dependence on angle. Consequently, an approximation to this solution is a medium with no angular dependence at all, an isotropic medium with a refractive index $n(0) \equiv n$. For this low-index spaceplate, $\mathcal{R} = (n_{\text{BG}}/n)$.

S2.1.2 Uniaxial spaceplate

We next consider the positive root $C = 0$ solution. Since the global phase offset is zero in this case, this spaceplate will mimic propagation for the purpose of imaging *and* interferometry. The refractive index ratio described by this solution is

$$\begin{aligned} \tilde{n}(\theta_{\text{SP}}) &= \frac{\pm \sqrt{\mathcal{R}^2(1 + \mathcal{R}^2 \tan^2 \theta_{\text{SP}})}}{(1 + \mathcal{R}^2 \tan^2 \theta_{\text{SP}}) \cos \theta_{\text{SP}}} \\ &= \frac{\pm \mathcal{R}}{\cos \theta_{\text{SP}} \sqrt{1 + \mathcal{R}^2 \tan^2 \theta_{\text{SP}}}}. \end{aligned} \quad (\text{S10})$$

Taking the positive root and using $\tilde{n} = n(\theta_{\text{SP}})/n_{\text{BG}}$, Eq. (S10) can be re-expressed in the standard form for the extraordinary index of a birefringent uniaxial crystal:

$$\begin{aligned} \frac{1}{n^2(\theta_{\text{SP}})} &= \frac{\cos^2 \theta_{\text{SP}} (1 + \mathcal{R}^2 \tan^2 \theta_{\text{SP}})}{n_{\text{BG}}^2 \mathcal{R}^2} \\ &= \frac{\cos^2 \theta_{\text{SP}}}{n_{\text{BG}}^2 \mathcal{R}^2} + \frac{\sin^2 \theta_{\text{SP}}}{n_{\text{BG}}^2} \\ &= \frac{\cos^2 \theta_{\text{SP}}}{n_o^2} + \frac{\sin^2 \theta_{\text{SP}}}{n_e^2}. \end{aligned} \quad (\text{S11})$$

The last line is valid if the crystal has its extraordinary axis along z , is negative uniaxial ($n_o > n_e$), $n_{\text{BG}} = n_e$, and $\mathcal{R} = n_o/n_e$. In this case, it will impart the ideal angle-dependent phase to mimic $d_{\text{eff}} = \mathcal{R}d$ of propagation in a medium with n_{BG} .

S2.1.3 Other solutions

Many other solutions are possible. For each value of $C \equiv C_+$, there is a positive root solution \tilde{n}_+ , *i.e.*, taking the $+$ sign in Eq. (S8). (Note, C_+ can be positive or negative.) Paired with this positive root solution there is a mirror negative root solution \tilde{n}_- , with $C = -C_+$. It is mirrored about the $\tilde{n} = 0$ line, in that the indices have the same magnitude but opposite sign, $\tilde{n}_- = -\tilde{n}_+$. A family of negative root solutions will have a refractive index that is positive for all angles, $\tilde{n}_-(\theta_{\text{SP}}) > 0$. We plot some of these solutions in Fig. S2c. Critically, it is unknown which index profiles $\tilde{n}(\theta_{\text{SP}})$ are physically allowable by Maxwell's equations.

S2.1.4 General properties of the solutions

We now consider some limiting cases for the angle-dependent spaceplate refractive index. We first consider a limit in which both C and \mathcal{R} become large. That is, we take $C' = tC$ and $\mathcal{R}' = t\mathcal{R}$ and take the large t limit:

$$\lim_{t \rightarrow \infty} \tilde{n}(\theta_{\text{SP}}) = \frac{\pm \sqrt{1 - \frac{C'^2}{\mathcal{R}'^2}}}{|\sin \theta_{\text{SP}}|}. \quad (\text{S12})$$

Consequently, in this limit, all the solutions have the same simple angular dependence up to an overall scaling factor.

Moreover, all the solutions, regardless of C and \mathcal{R} , will fall between these two curves:

$$\lim_{\mathcal{R} \rightarrow \infty} \tilde{n}(\theta_{\text{SP}}) = \frac{\pm 1}{|\sin \theta_{\text{SP}}|}, \quad (\text{S13})$$

indicated by the black dashed curves in Fig. S2. The compression factor and C parameter can be expressed in terms of the value of \tilde{n} at two angles. First, at normal incidence,

$$\tilde{n}(\theta_{\text{SP}} = 0^\circ) = C \pm \mathcal{R}. \quad (\text{S14})$$

Second, while not all solutions give a real-valued refractive index ratio out to $\theta_{\text{SP}} = 90^\circ$, for those that do,

$$\tilde{n}(90^\circ) = \pm \sqrt{1 - \frac{C^2}{\mathcal{R}^2}}. \quad (\text{S15})$$

Consequently, in terms of these two boundaries values of \tilde{n} , the compression factor is given by,

$$\mathcal{R} = \pm \tilde{n}(0^\circ) \left(1 \pm \sqrt{1 - \frac{1}{(\tilde{n}(90^\circ))^2}} \right). \quad (\text{S16})$$

S3 Fabricated spaceplates

The low-index spaceplate was fabricated by attaching microscope cover slips to both ends of a lens tube using epoxy (Fig. S3a). The uniaxial spaceplate was fabricated by a commercial vendor, which informed us that, in calcite, surfaces normal to the extraordinary axis are difficult to polish well (Fig. S3b). Consequently, some roughness can be observed on the entrance and exit surfaces, resulting in scattering, particularly in the beam measurements.

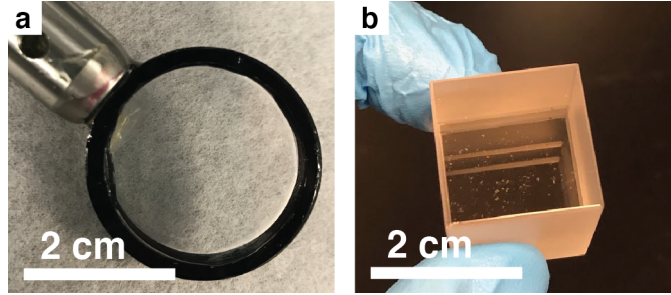


Fig. S3 | Fabricated spaceplates. **a**, Low-index spaceplate. **b**, Uniaxial spaceplate. The entrance and exit surfaces exhibit visible roughness.

S4 Evidence for a fully two-dimensional spaceplate effect

All three spaceplate types that we have introduced function in both transverse directions, x and y . That is, the spaceplate advances the propagation of the full two-dimensional spatial distribution of the light-field. To demonstrate this, in this section, we present the same measurement as done in Fig. 2a but now projecting the beam along y . Consequently, the plot-vertical gives the intensity distribution along y .

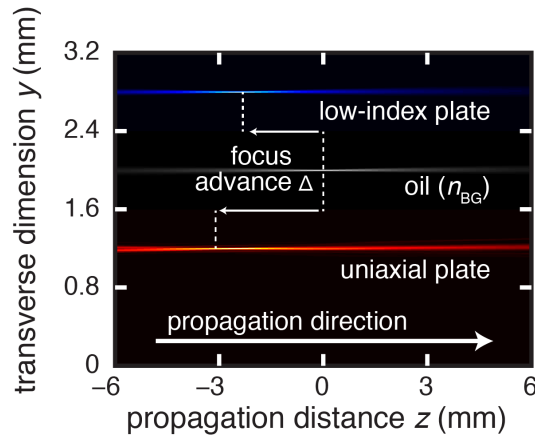


Fig. S4 | Experimental demonstration of space compression. The colour along the plot-vertical gives the transverse intensity distribution along y at each point along the horizontal plot axis for all plots.

a, Focal shift, $\Delta = d - d_{\text{eff}}$. Middle data: Oil (grey). A converging beam comes to focus in oil at $z = 0$. Top data: Low-index spaceplate (blue). Propagation through a plate of air advances the focus position along z by $\Delta = -2.3$ mm. Bottom data: Uniaxial spaceplate (red). Propagation of an extraordinary polarized beam through a calcite crystal with its fast axis along z advances the focus position by $\Delta = -3.4$ mm.

S5 Polarization measurements

In this section, we present measurements on polarized beams with the uniaxial spaceplates. Using the polarization control detailed in the Methods section of the main paper and in Sec. S1, we repeat the beam measurements with an ordinarily polarized beam. While for extraordinarily polarized light the uniaxial crystal acts as a spaceplate, for ordinarily polarized light it acts a homogeneous isotropic medium with refractive index $n_o > n_{BG}$. Consequently, it acts in the opposite manner to a spaceplate; this must be compensated with more propagation distance in a given setup. We measured the uniaxial crystal's effect on the focal shift of an ordinarily polarized beam and, also, on the beam's lateral shift when the spaceplate is tilted. The experimental results are shown in Fig. S5. The focal shift observed for the ordinarily polarized beam was $\Delta = 3.2$ mm away from the crystal which agrees well with the theoretical shift $\Delta = -(\mathcal{R} - 1)d = 3.126$ mm for $\mathcal{R} = n_{BG}/n_o = 0.895$.

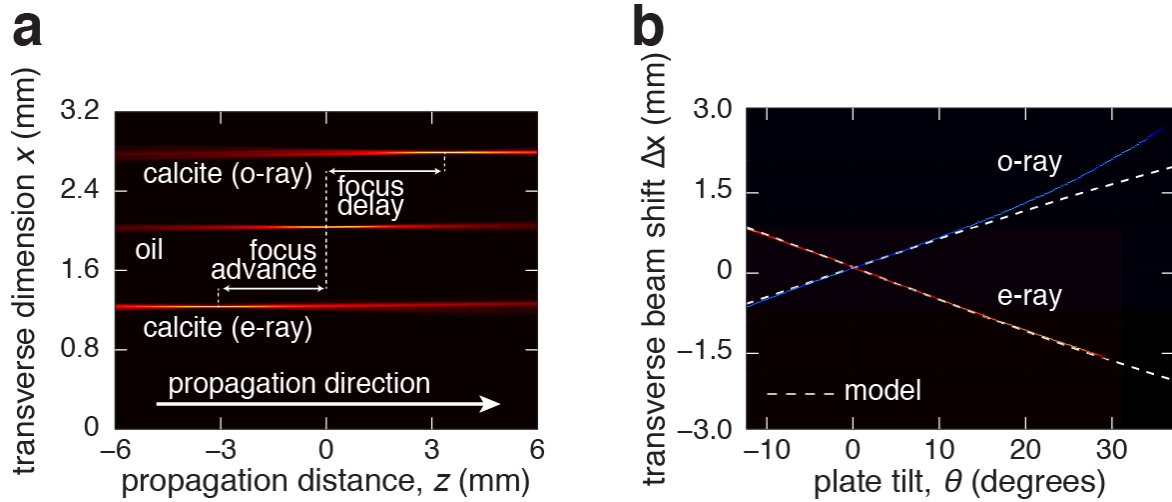


Fig. S5 | Polarized beam measurements with the uniaxial spaceplate. With an extraordinarily (e-ray) polarized beam, we repeated the calcite measurements reported in Fig. 2 (see the main paper for details). For comparison, we also include the results for an ordinarily (o-ray) polarized beam. **a**, Focal shift Δ along z . Relative to the focus location in the absence of a spaceplate (oil), the o-ray has its focus shifted further from the spaceplate, *i.e.*, delayed. The spaceplate effect is evident in the e-ray, which has its focus advanced towards the spaceplate. **b**, The lateral shift Δx of a beam due to tilting the uniaxial spaceplate by θ relative to the z -axis. The o-ray shifts in opposite manner to what is required by a spaceplate, in contrast to the e-ray. The dashed lines are Δx for an ideal spaceplate with (e-ray) compression factor $\mathcal{R} = n_o/n_e = 1.117$ matching calcite and (o-ray) $\mathcal{R} = n_{BG}/n_o = 0.895$. Notice that the lateral shift of the o-ray deviates from the approximately straight theory line whereas the e-ray does not. This deviation is evidence of the aberrations that ordinarily polarized light will encounter. In contrast, the uniaxial crystal operates ideally for all angles.

S6 Transverse and lateral beam shifts due to a spaceplate

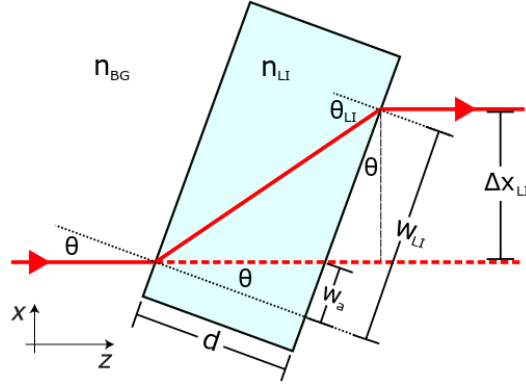


Fig. S6 | Geometry for the derivation of lateral beam shift Δx_{LI} in the case of a low-index plate.

As depicted in Fig. 1a in the paper, one expects a spaceplate to shift a beam of light when incident at an angle θ . In this section, we derive the transverse shift w and lateral shift Δx . We first derive the shift due to propagating through a slab of medium n_{BG} of thickness d_{eff} , which defines the effect of an ideal spaceplate. We then derive these shifts for the low-index spaceplate and uniaxial spaceplate.

S6.1 Beam shifts due to an ideal spaceplate

Consider a beam traveling in the x, z plane at an angle θ to the z -axis. The beam traverses a region (*i.e.*, a slab) of a medium at length $z = d_{eff}$, entering at point $(x_{in}, z = 0)$ and exiting at point $(x_{out}, z = d_{eff})$. Upon exiting the region the beam is parallel to the beam that entered the region. That is, its angle is unchanged.

By simple geometry the beam shifts in the x -direction by an amount,

$$x_{out} - x_{in} = -d_{eff} \tan \theta \equiv w, \quad (S17)$$

which we name the ‘transverse’ shift. The negative sign is due to a convention that will be explained in the next paragraph. For an ideal spaceplate, the same beam will exit translated along the plate’s interface by an equal amount w of transverse shift as created by the slab of medium described above. Another way of looking at the transverse shift is as a displacement from a line that both goes through point $(x_{in}, z = 0)$ and is normal to the plate interfaces. In contrast to the scenario with the medium, this shift now occurs at a distance $z = d$, the plate thickness.

To test this effect, rather than tilt the incoming beam by θ , it is experimentally simpler to tilt the studied spaceplate by the same angle. In this case, the quantity that can be measured most directly is the ‘lateral’ shift Δx of the beam. This is the shift of the beam along an axis normal to the beam’s propagation direction. The sign convention mentioned in the last paragraph sets Δx to be positive if the lateral shift is below the path of the incident beam, as depicted in Fig. S6. In particular, Δx would be positive for a beam passing through a tilted regular glass plate in a vacuum background medium.

To relate Δx to w , one must account for the tilt of the normal of the plate interface. This alone would result in apparent transverse shift of $w_a = d \tan \theta$, which must be added to the actual transverse shift w . With this established, geometry gives the lateral shift as,

$$\begin{aligned} \Delta x &= (w + w_a) \cos \theta \\ &= (-d_{eff} \tan \theta + d \tan \theta) \cos \theta \\ &= -d (\mathcal{R} - 1) \sin \theta, \end{aligned} \quad (S18)$$

where we have used $d_{\text{eff}} = \mathcal{R}d$.

S6.2 Beam shifts due to a low-index spaceplate

We now consider the lateral shift created by a plate made of an isotropic and homogeneous medium of thickness d . If the medium's refractive index $n_{\text{LI}} < n_{\text{BG}}$, then the plate is a low-index spaceplate. To start, however, we leave n_{LI} unrestricted. At the entrance interface, incoming light refracts to angle θ_{LI} inside the plate according to Snell's law. In the following, we use Snell's law to derive analogous relations for cos and tan:

$$\begin{aligned}\sin \theta_{\text{LI}} &= \frac{n_{\text{BG}}}{n_{\text{LI}}} \sin \theta, \\ \cos \theta_{\text{LI}} &= \sqrt{1 - \sin^2 \theta_{\text{LI}}} = \sqrt{1 - \left(\frac{n_{\text{BG}}}{n_{\text{LI}}}\right)^2 \sin^2 \theta}, \\ \tan \theta_{\text{LI}} &= \frac{\sin \theta_{\text{LI}}}{\cos \theta_{\text{LI}}} = \frac{\frac{n_{\text{BG}}}{n_{\text{LI}}} \sin \theta}{\sqrt{1 - \left(\frac{n_{\text{BG}}}{n_{\text{LI}}}\right)^2 \sin^2 \theta}} = \frac{\sin \theta}{\sqrt{\left(\frac{n_{\text{LI}}}{n_{\text{BG}}}\right)^2 - \sin^2 \theta}}.\end{aligned}\tag{S19}$$

As in Eq. (S17) from the last section, simple geometry shows that the transverse shift of the beam is,

$$w_{\text{LI}} = -d \tan \theta_{\text{LI}}.\tag{S20}$$

Likewise, the lateral shift is,

$$\begin{aligned}\Delta x_{\text{LI}} &= (w_{\text{LI}} + w_a) \cos \theta \\ &= (-d \tan \theta_{\text{LI}} + d \tan \theta) \cos \theta.\end{aligned}\tag{S21}$$

Substituting Eq. (S19) into Eq. (S21) yields an expression for the lateral shift that is dependent only on θ ,

$$\Delta x_{\text{LI}} = -d \sin \theta \left(\frac{\cos \theta}{\sqrt{\left(\frac{n_{\text{LI}}}{n_{\text{BG}}}\right)^2 - \sin^2 \theta}} - 1 \right).\tag{S22}$$

This shows that the lateral shift created by a low-index spaceplate is not equal to the ideal lateral shift given in Eq. (S18). However, using the small angle approximation ($\theta \ll 1$) we find that

$$\begin{aligned}\Delta x_{\text{LI}} &\approx -d \sin \theta \left(\frac{1}{\sqrt{\left(\frac{n_{\text{LI}}}{n_{\text{BG}}}\right)^2 - 0}} - 1 \right) + O(\theta^3) \\ &= -d \sin \theta \left(\left| \frac{n_{\text{BG}}}{n_{\text{LI}}} \right| - 1 \right) \\ &= -d (\mathcal{R} - 1) \sin \theta \\ &= \Delta x,\end{aligned}\tag{S23}$$

where we have identified the low-index compression factor, $\mathcal{R} = |n_{\text{BG}}/n_{\text{LI}}|$. For large angles, the low-index spaceplate will produce an incorrect shift, effectively introducing aberrations. Moreover, all angles above

the critical angle, $\theta_c = \arcsin(n_{\text{LI}}/n_{\text{BG}})$, are perfectly reflected. However, for small angles a low-index plate acts as an ideal spaceplate, *i.e.*, $\Delta x_{\text{LI}} = \Delta x$.

While we have derived the lateral shift Δx_{LI} in the context of a low-index spaceplate, it is actually valid for any value of n_{LI} , including a negative refractive index. Moreover, we use it to describe the action of the uniaxial spaceplate on ordinarily polarized light, which effectively experiences a homogeneous isotropic medium with index n_o . Lastly, the shift Δx_{LI} also shows that a simple glass plate in air will introduce imaging aberrations for large angles.

S6.3 Beam shifts due to a uniaxial spaceplate

We will now derive the lateral shift created by a uniaxial spaceplate. The uniaxial crystal is characterized by two indices, the extraordinary and ordinary refractive indices, n_e and n_o , respectively. To derive the shift, one must account for the anomalous refraction and consequent beam walk-off that generally occurs with a birefringent medium. In particular, for extraordinarily polarized light in a uniaxial crystal (U), the Poynting vector $\vec{S}^{(\text{U})}$, which describes the energy flow, can point in a direction different from the wavevector $\vec{k}^{(\text{U})}$. In contrast, an ordinarily polarized beam will refract normally (*i.e.*, the Poynting and wavevectors are parallel), and, hence, will shift according to Eq. (S23) but with n_{LI} replaced with n_o . In the following, we use the results from Ref. [51], which carefully analyzed the Poynting vector angle at the interface between a homogeneous medium and a uniaxial crystal with its extraordinary axis (*i.e.*, optic axis) at an arbitrary angle. Since the Poynting vector is the direction an extraordinary beam travels along in the crystal, one can use it to follow a geometric derivation similar to that used in Eq. (S18).

As discussed earlier in the SI, the transverse component of the wavevector is conserved across the interface,

$$k_{\perp}^{(\text{U})} = k_{\perp}^{(\text{BG})} \equiv k_{\perp} = k_0 n_{\text{BG}} \sin \theta. \quad (\text{S24})$$

We apply the results from Ref. [51] to the case where the extraordinary axis is normal to the plate interface. In this case, the z -component of the wavevector in the crystal can be expressed as:

$$k_z^{(\text{U})} = n_o k_0 \sqrt{1 - \left(\frac{n_{\text{BG}}}{n_e}\right)^2 \sin^2 \theta}. \quad (\text{S25})$$

If one considers the case where $n_{\text{BG}} = n_e$, then $k_z^{(\text{U})} = n_o k_0 \cos \theta$, which directly shows why a uniaxial crystal acts as a spaceplate: it produces an angle-dependent phase that is magnified by a factor n_o/n_e relative to propagation through a medium with $n_{\text{BG}} = n_e$. For now, however, we leave n_e general.

Whereas, after refraction at the interface, the wavevector angle in the crystal will be given by $\tan \theta_{\text{U},k} = k_{\perp}^{(\text{U})}/k_z^{(\text{U})}$, Ref. [51] showed that the Poynting vector of an extraordinarily polarized plane-wave will be along a potentially different angle,

$$\begin{aligned} \tan \theta_{\text{U},S} &= \frac{n_o^2 k_{\perp}^{(\text{U})}}{n_e^2 k_z^{(\text{U})}} \\ &= \frac{n_o^2 k_0 n_{\text{BG}} \sin \theta}{n_e^2 n_o k_0 \sqrt{1 - \left(\frac{n_{\text{BG}}}{n_e}\right)^2 \sin^2 \theta}}, \end{aligned}$$

where we have used the expressions for the two wavevector components, Eqs. (S24) and (S25).

From here on, we restrict ourselves to the case in which $n_{\text{BG}} = n_e$. In this case, the Poynting vector angle reduces to

$$\tan \theta_{\text{U},S} = \mathcal{R} \tan \theta, \quad (\text{S26})$$

where we have identified the compression factor as $\mathcal{R} = n_o/n_e$, as expected from our phase analysis earlier. Using Eq. (S26), the transverse shift for an extraordinarily polarized beam will be

$$w_U = -d\mathcal{R} \tan \theta, \quad (\text{S27})$$

which can be used to find the associated lateral shift:

$$\begin{aligned} \Delta x_U &= (w_U + w_a) \cos \theta \\ &= (-d \tan \theta_{U,S} + d \tan \theta) \cos \theta \\ &= -d(\mathcal{R} - 1) \sin \theta \\ &= \Delta x. \end{aligned} \quad (\text{S28})$$

This shows that for all angles, the lateral shift of an extraordinarily polarized beam Δx_U will be identical to the lateral shift of an ideal spaceplate Δx . In this sense, a uniaxial crystal acts as a perfect spaceplate for the purposes of imaging, replacing medium n_{BG} , while introducing no aberrations.

S7 Spaceplate metamaterial

The metamaterial is designed for operation at an optical wavelength of $\lambda = 1550$ nm. At this wavelength, the complex refractive index of silicon is $n_{Si} = 3.48985 + 0.00982674i$, and the refractive index of silica glass is $n_{SiO_2} = 1.45611$. The device has 25 layers and a total thickness of $10.1752 \mu\text{m}$. Table 1 lists the individual layer thicknesses; Figure S7 depicts the cross-section of the metamaterial to scale.

The values in the Table 1 are listed up to 3 decimal places, as was produced by the genetic algorithm. As can be inferred by the convergence test shown in Fig. S9, the device is robust to fabrication imperfections, and so this level of precision is not necessary to generate a metamaterial spaceplate that demonstrates a focus advance.

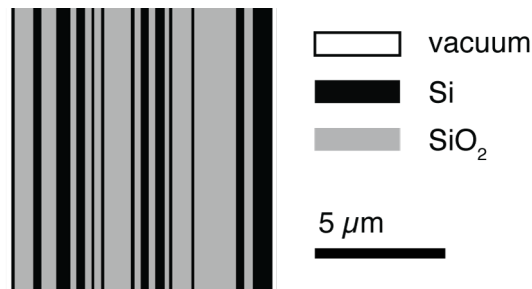


Fig. S7 | Schematic of the nonlocal metamaterial spaceplate. The spaceplate consists of a multilayer stack formed of two materials, silicon (Si) and silicon dioxide (SiO_2). The schematic is to scale for the given scalebar.

Layer	Material	Thickness (nm)	Layer	Material	Thickness (nm)	Layer	Material	Thickness (nm)
1	Si	133.86	10	SiO ₂	265.555	18	SiO ₂	168.605
2	SiO ₂	722.324	11	Si	124.592	19	Si	125.935
3	Si	319.406	12	SiO ₂	1032.82	20	SiO ₂	747.517
4	SiO ₂	573.293	13	Si	145.7	21	Si	105.681
5	Si	551.083	14	SiO ₂	239.521	22	SiO ₂	1629.52
6	SiO ₂	232.074	15	Si	313.439	23	Si	318.601
7	Si	340.955	16	SiO ₂	252.054	24	SiO ₂	334.673
8	SiO ₂	254.686	17	Si	371.439	25	Si	766.62
9	Si	105.252						

Table 1. Materials and thicknesses of individual layers in the metamaterial spaceplate shown in Fig. S7.

Figure S8 demonstrates the performance of the metamaterial spaceplate for both p-polarized and s-polarized focusing Gaussian beams for operating wavelengths ranging from 1530 nm to 1560 nm.

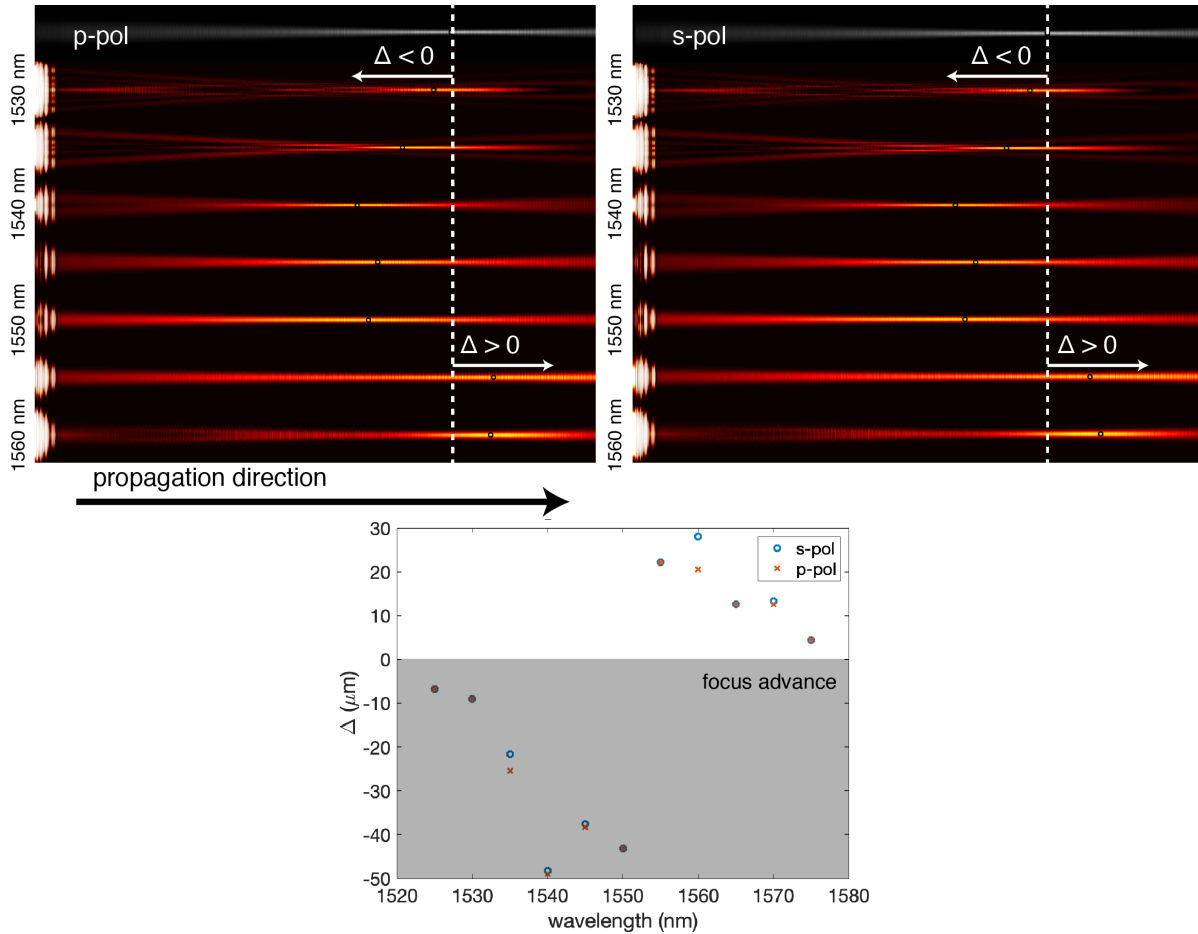


Fig. S8 | Broadband operation of the metamaterial spaceplate. **Top**, full-wave simulations of the magnitude of the electric field $|E|^2$ of a focusing Gaussian beam propagating in vacuum (grey, top row) and after propagating through the metamaterial for a range of operating wavelengths (red, all rows but the top row). The device generates a focus advance ($\Delta < 0$) for both polarizations and for wavelengths ranging from 1530 – 1560 nm. **Bottom**, the total focus advance Δ as a function of wavelength for this device.

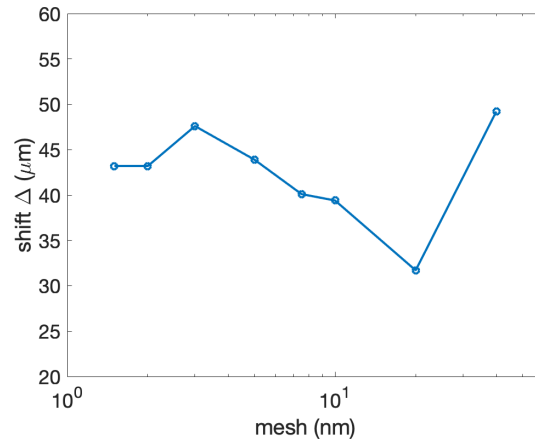


Fig. S9 | Mesh convergence test for the finite-difference time-domain simulation. The shift of the focus Δ relative to vacuum is simulated as a function of the smallest mesh size along the direction of propagation within the metamaterial. Here, the smallest mesh used was 2 nm. Critically, all these simulations show a sizeable negative shift and, thus, exhibit the spaceplate effect.